APPLIED SCIENCES AND ENGINEERING

Organ-on-e-chip: Three-dimensional self-rolled biosensor array for electrical interrogations of human electrogenic spheroids

Anna Kalmykov[1], Changjin Huang[2,3], Jacqueline Bliley[1], Daniel Shiwarski[1], Joshua Tashman[1], Arif Abdullah[4], Sahil K. Rastogi[1], Shivani Shukla[1,5], Elnatan Mataev[1], Adam W. Feinberg[1,5], K. Jimmy Hsia[2,3], Tzahi Cohen-Karni[1,5]*

Cell-cell communication plays a pivotal role in coordination and function of biological systems. Three-dimensional (3D) spheroids provide venues to explore cellular communication for tissue development and drug discovery, as their 3D architecture mimics native in vivo microenvironments. Cellular electrophysiology is a prevalent signaling paradigm for studying electroactive cells. Currently, electrophysiological studies do not provide direct, multisite, simultaneous investigation of tissues in 3D. In this study, 3D self-rolled biosensor arrays (3D-SR-BAs) of either active field-effect transistors or passive microelectrodes were implemented to interface human cardiac spheroids in 3D. The arrays provided continuous and stable multiplexed recordings of field potentials with high sensitivity and spatiotemporal resolution, supported with simultaneous calcium imaging. Our approach enables electrophysiological investigation and monitoring of the complex signal transduction in 3D cellular assemblies toward an organ-on-an-electronic-chip (organ-on-e-chip) platform for tissue maturation investigations and development of drugs for disease treatment, such as arrhythmias.

INTRODUCTION

Cell-cell communication is fundamental to multicellular life and to the emergence of higher-order functions in a wide variety of tissues and organs. In their native three-dimensional (3D) environment, cells are intimately connected to each other and the surrounding matrix to form a complex and highly dynamic system (*1*). Culturing cells on two-dimensional (2D) surfaces has been the foundation of in vitro cell culture for decades. However, 2D culturing environment and native 3D tissue environment are not only different quantitatively (e.g., in dimensions) but, more importantly, also different qualitatively in many key characteristics of cellular behaviors (*2*). Specifically, 2D-cultured cells show distinctly different cellular morphology (*2*), proliferation rates (*3*), cell–extracellular matrix interactions (*4*), migration (*5*), gene expression (*6*), differentiation (*7*), signaling (*8*), physiological function (*9*), and electrophysiological properties (*1*).

Cellular electrophysiology is a prevalent paradigm used to study cellular communication across a wide range of cells, from electroactive cells such as cardiomyocytes (CMs), neurons, or α/β cells in pancreatic islets, to non-electroactive cells, such as hepatocytes, and immune cells. 3D organoid-based systems, such as organ-on-a-chip platforms, are new venues for tissue development exploration and drug discovery (*10*). Properly characterizing the physiological properties of such systems would pave the way for improved understanding of the mechanisms underlying cell-cell communication and potential applications in tissue engineering. Currently, electrophysiological studies of cells and tissues are carried out using a variety of techniques, including glass micropipette patch-clamp electrodes (*11*), voltage- and Ca^{2+}-sensitive dyes (*12*), multielectrode arrays (MEAs) (*13*), and planar field-effect transistors (FETs) (*14*). However, direct, multisite, simultaneous, and native-like topology (3D) electrophysiological investigation has not been demonstrated in spheroid-based tissues. Specifically, the voltage- and ion-sensitive dyes may be toxic to the cells and are currently limited in volumetric (3D) measurements (*12*). The patch-clamp technique is limited by its recording sites (*11*), and its use in multiplexed recording from spheroids has not been demonstrated. While the microfabricated planar (2D) FETs (*14*) and MEAs (*15*) allow multiplexed detection on a scale not possible with micropipette technology (*16*), both MEAs and FETs are confined to 2D substrates that renders 3D electrical recording immensely challenging (Fig. 1) (*17*). Recently, 3D bioelectrical interfaces were reported. For example, a porous conductive polymer, poly(3,4-ethylenedioxythiophene):poly(sodium 4-styrenesulfonate) (PEDOT:PSS), acted both as a transistor channel and as a scaffold monitored cell attachment in 3D (*18*). 3D MEAs were demonstrated to wrap around individual cell's surface and obtain electrophysiological recordings with subcellular resolution (*17*). However, multicellular tissue-scale, 3D multisite, and simultaneous recordings have not been previously demonstrated.

Here, we present a novel approach, an organ-on-electronic-chip (organ-on-e-chip), a 3D self-rolled biosensor array (3D-SR-BA), for electrophysiological measurements of spheroids that enables the study of cell-cell communications of 3D multicellular systems (Fig. 1). Self-rolled polymeric structures have been obtained in recent years (*17*, *19*). Main actuation mechanisms include light, pH, temperature, and electrical or magnetic triggering. Our idea of controlled assembly of electrical biosensors in 3D is presented in Fig. 1. We choose to use a prestressed metal/polymer support multilayer structure as our working system. The self-rolling platform is fabricated on a planar surface (Fig. 1A), and once released off the surface, it achieves a

[1]Department of Biomedical Engineering, Carnegie Mellon University, Pittsburgh, PA 15213, USA. [2]School of Mechanical and Aerospace Engineering, Nanyang Technological University, 639798 Singapore, Republic of Singapore. [3]School of Chemical and Biomedical Engineering, Nanyang Technological University, 639798 Singapore, Republic of Singapore. [4]Department of Mechanical Science and Engineering, University of Illinois at Urbana-Champaign, Urbana-Champaign, IL 61801, USA. [5]Department of Materials Science and Engineering, Carnegie Mellon University, Pittsburgh, PA 15213, USA.
*Corresponding author. Email: tzahi@andrew.cmu.edu

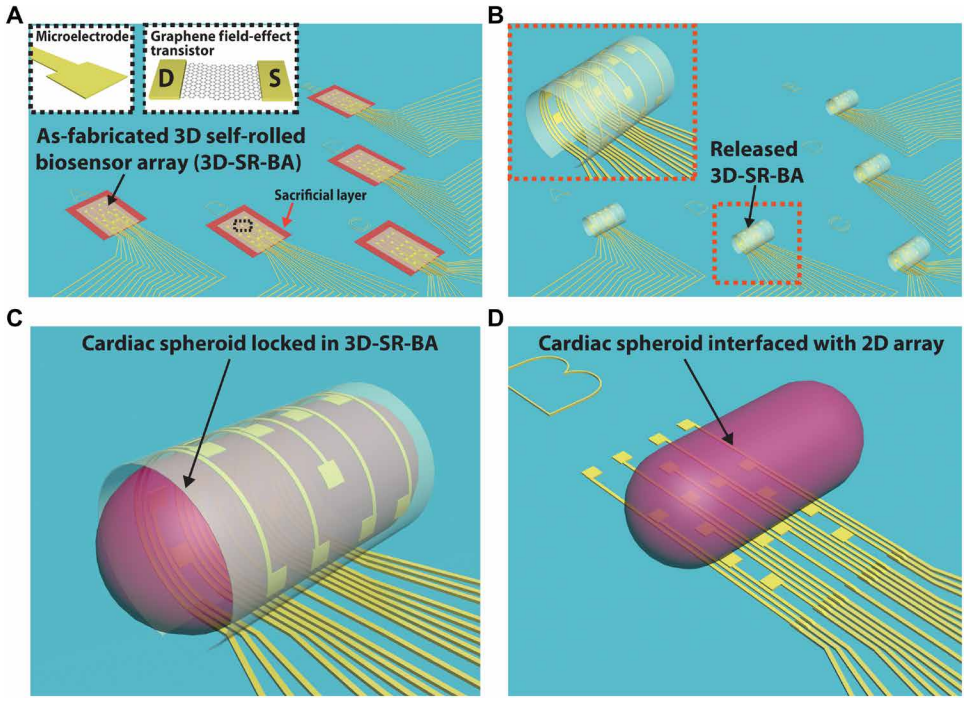

Fig. 1. 3D-SR-BAs for electrical interrogation of human electrogenic spheroids. (**A**) 3D-SR-BAs are fabricated using conventional lithography techniques on a sacrificial layer (red arrow). Inset, expanded view of the marked black dashed box of either passive (microelectrode) or active [graphene field-effect transistor (GFET)] biosensors. S and D denote source and drain of the GFET, respectively. (**B**) Leveraging the prestress in the metal interconnects (gold colored traces), the arrays self-roll upon removal of the sacrificial layer. Inset, expanded view of the marked red dashed box. (**C**) Cardiac spheroids encapsulated in the 3D-SR-BAs, allowing electrical measurements in 3D. (**D**) The interface between the cardiac spheroid and array in 2D provides a limited interface for electrical measurement only from the apex of the spheroids.

controlled 3D geometry (Fig. 1B). We applied the approach to study the propagation of electrical signals within stem cell–derived engineered cardiac spheroids, an ideal system to test the approach performance due to the unmet need in understanding the cell-cell communication processes in this 3D cellular spheroid system (Fig. 1C) (*20*). The presented 3D-SR-BAs provide a novel tool to record electrophysiological signals of native 3D tissue organization to aid the understanding of signal transduction in complex cellular assemblies. Knowing how electrical information propagates in a spheroid will greatly affect our basic understanding of signal transduction in complex cellular assemblies. This will shed light on the relationship between electrical signals and disease, such as arrhythmias, and will enable an organ-on-e-chip platform for tissue maturation investigations as well as further development and assessment of the efficacy of drugs for disease treatment, such as arrhythmias.

RESULTS AND DISCUSSION

Highly controlled 3D-SR-BAs

The power of our 3D sensing device lies in its tunable characteristics, controlled not only by the arrangements of the electrodes but also by the curvature of the device. The self-rolled device allows 3D measurements of tissue-scale electrophysiology (Fig. 1C) that are not accessible with conventional electronics, fabricated on 2D chip surfaces. An interface of a 3D native tissue with a 2D measurement platform is limited, as a tight tissue-sensor interface can only be achieved on the apex of the tissue, as shown in Fig. 1D. Measuring the electrical activity of the entire 3D construct from all sides provides a unique opportunity to gain understanding of signal propagation in the total construct. To achieve this mode of electrophysiological study, this work develops the 3D-SR-BA. By strategically placing the electrodes and adjusting the rolled-up curvature, the 3D-SR-BA devices have the potential to provide substantially richer information about electrophysiological behavior of cell clusters and tissues. To trigger such self-rolling, we fabricated the 3D-SR-BAs (see Materials and Methods) on a sacrificial layer and polymeric support with metallic electrode lines that provide source and drain interconnects to the FETs, as illustrated by Fig. 2A. The arrays obtained a 3D conformation upon etching off the sacrificial layer as they spontaneously self-rolled (Fig. 2, B and C, and movie S1). To achieve a desired curvature, mechanics and mechanical properties of the materials used to construct these devices play a central role (*21*). Similar to the devices with semiconductor thin films demonstrated by Li and co-workers (*22*), the shape transformation of 3D-SR-BAs is driven by the residual mismatch stress between different constituent layers. While the residual stress in SU-8 layers is negligible (*14*), substantial tensile stresses can be generated in the Pd and Cr layers (*23*, *24*). The residual stress level in metal thin films at the nanoscale largely depends on both the film thickness and the fabrication process. Such residual stress can be controlled by varying deposition pressure, deposition rate, and final film thickness (*23*, *24*). Varying the SU-8 layer thickness in these structures further modulates the radius of curvature. The exact amount of the residual stress is not easy to measure experimentally (*25*), but the effects of the residual stresses can be studied by numerical mechanics analysis. A systematic 3D finite element analysis (FEA) was performed to understand the self-rolling behavior of the 3D-SR-BAs. The thickness and mechanical properties of different constituent layers are

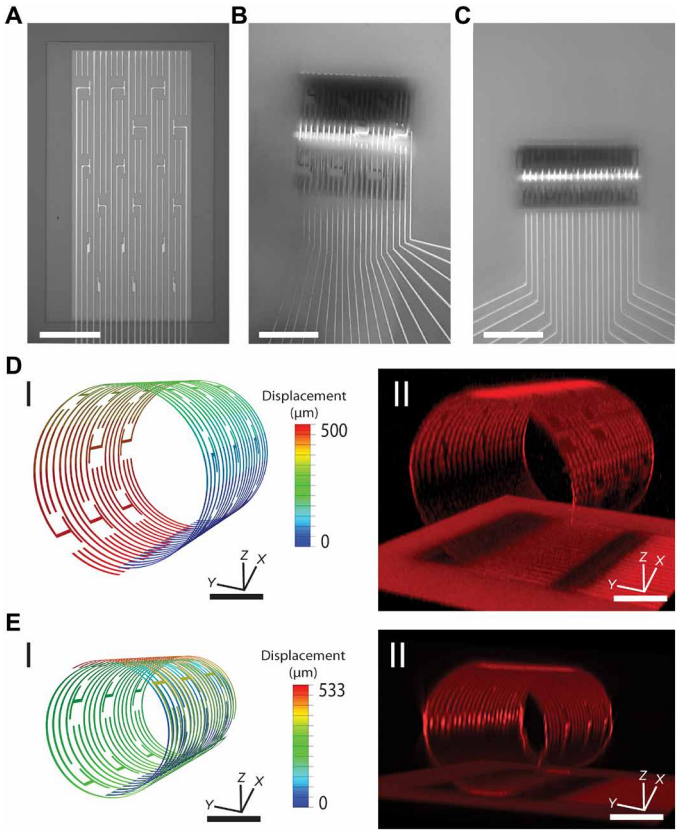

Fig. 2. Highly controlled 3D-SR-BAs. (**A** to **C**) Bright-field optical microscopy images of photolithographically fabricated 3D-SR-BAs. (A) As fabricated 3D-SR-BA before being released. (B) 3D-SR-BA released with a single turn. (C) 3D-SR-BA released with ~1.7 turns. Scale bars, 100 μm. (**D** and **E**) 3D-SR-BAs with varying radii of curvature — simulation and experimental results. (D) 3D-SR-BA with a single turn. (I) A finite element analysis (FEA) simulation result for a 3D-SR-BA with a single turn (inner diameter of ~160 μm). Color bar represents the magnitude of the displacement of the 3D-SR-BA upon removal of the sacrificial layer; SU-8 layers are not shown for visual purpose. (II) A 3D confocal microscopy image of a representative 3D-SR-BA with a single turn ($n = 9$). (E) 3D-SR-BA with multiple turns. (I) FEA simulation result for a 3D-SR-BA with ~1.7 turns (inner diameter, ~100 μm). Color bar represents the magnitude of the displacement of the 3D-SR-BA upon removal of the sacrificial layer; SU-8 layers are not shown for visual purpose. (II) 3D confocal microscopy image of a representative 3D-SR-BAs with ~1.7 turns ($n = 15$). Scale bars, 50 μm.

summarized in table S1. In all the simulations, a thicker bottom SU-8 layer and a relatively thinner top SU-8 layer were adopted to achieve a directional rolling. This residual stress-induced self-rolling behavior was modeled as a differential thermal expansion-driven shape transformation problem, with further details of the simulations listed in Materials and Methods.

The simulations allow the prediction of the final configurations of the 3D-SR-BAs after dissolving the sacrificial layer (Fig. 2). Representative images of the experimental results for 3D-SR-BAs self-rolled in a single turn with an inner diameter of ~160 μm (Fig. 2, B and D, II) and ~1.7 turns with an inner diameter of ~100 μm (Fig. 2, C and E, II) illustrate the highly controlled arrays' geometry. The degree of rolling of the 3D-SR-BAs, characterized by their radius of curvature (fig. S2A), is simultaneously regulated by the geometric design and the residual stress level in metal films, as shown in fig. S2, B and C. For a specific design, a higher residual stress in the top Cr layer promotes rolling behavior, leading to a reduced radius of curvature (fig. S2B). Matching the radius of curvature observed in experiments with that in the simulations allows the estimation of an average residual stress in the top Cr layer at 1.1 GPa. Upon determination of the residual stress, the desired rolled configurations were achieved by manipulating the thicknesses of the top and bottom SU-8 layers. As demonstrated in fig. S2C, increasing the thickness of either the top or bottom SU-8 layer suppresses the rolling capability, leading to a rolled configuration with an increased radius of curvature. The specific geometric designs to obtain a single turn and ~1.7 turns were identified from simulations and successfully verified in the experiments, as shown in Fig. 2 (D and E, respectively). The high correlation between the simulated radius of curvature (Fig. 2, D, I, and E, I) and the experimental results (Fig. 2, D, II, and E, II) demonstrates how variation of the experimental parameters can precisely control the 3D-SR-BAs' curvature. This allows direct monitoring of electrical activity of 50- to 200-μm-diameter spheroids, thus improving the biosensor-cell interface while maintaining the spheroids' integrity (*16*).

Biosensors on 3D-SR-BA

The 3D-SR-BA platform is flexible and can accommodate a variety of sensor types to be used in either electrophysiological investigation of tissue state or detection of biomolecules released by the tissue. The main categories of sensors are active sensors, such as FETs, that provide the benefit of high sensitivity with potential use in biosensing, and passive sensors, such as MEAs, which allow a two-way interaction with the cells with potential applications in both recording and stimulating cell responses (*16*). The focus of this study is the 3D assembly of microelectrodes. To illustrate the flexibility of the 3D-SR-BA, we also demonstrate the fabrication of graphene FETs (GFETs) on 3D-SR-BA.

3D-SR-BAs with passive biosensors: Microelectrodes

MEA, a technology used to study the electrophysiology of cellular networks, enables not only multisite recording but also precise electrical stimulation (*17*). MEAs were fabricated on 3D-SR-BAs (see Materials and Methods) and assembled in 3D to interrogate the electrical activities of the spheroids with cellular resolution, as illustrated by the 3D confocal image (Fig. 3A). Briefly, an array of 25 μm × 25 μm Au electrodes was fabricated on the 3D-SR-BA (fig. S1B), followed by metallization with Cr/Pd/Cr/Au and electrode passivation. The radius of curvature of 3D-SR-BA with microelectrodes was highly controlled by changing the fabrication parameters (Fig. 3A and fig. S3, A to C). To characterize the electrochemical properties of the microelectrodes, cyclic voltammetry (CV) and electrochemical impedance spectroscopy (EIS) were performed in a three-electrode electrochemical cell (Fig. 3, B and C) (*15*). The microelectrodes can weakly resolve the oxidation and reduction peaks of the potassium hexacyanoferrate(III), $K_3[Fe(CN)_6]$, which is a typical observation for electrodes at that size (fig. S3D, blue trace) (*15*). Sweeping the potential across the working electrode (i.e., the microelectrode) in KCl leads to a featureless capacitive current curve due to the electrical double-layer formation (Fig. 3B, blue trace). The microelectrodes were further modified with PEDOT:PSS to reduce their impedance and thus improve the recording (*26*). PEDOT:PSS-modified electrodes exhibited improved capacitance due to electrical double-layer formation at the interconnected PEDOT- and PSS-rich grains (Fig. 3B, red trace) (*27*). The modified microelectrodes were able to resolve the oxidation and reduction peaks of $K_3[Fe(CN)_6]$ (fig. S3D,

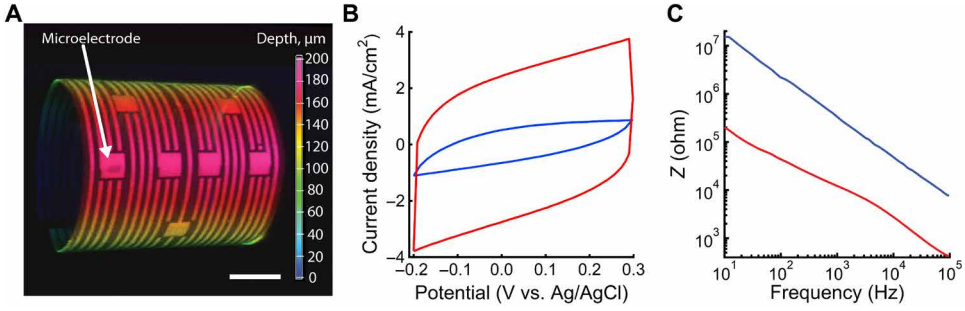

Fig. 3. 3D-SR-BA with functional passive biosensors (microelectrodes). (**A**) 3D confocal microscopy image of 3D-SR-BA with microelectrodes. Color bar represents the depth in micrometers. Scale bar, 50 μm. (**B**) Representative cyclic voltammograms (CV) acquired with 1 M KCl at 600 mV/s before (blue trace) and after (red trace) PEDOT:PSS electrodeposition ($n = 10$). (**C**) Electrochemical impedance spectroscopy (EIS) plots for the electrodes before (blue trace) and after (red trace) PEDOT: PSS electrodeposition ($n = 23$).

red trace), indicating that the biosensors are electrochemically active. To further characterize the impedance of the electrodes before and after PEDOT:PSS electrodeposition, we performed EIS. The Au microelectrodes pre-electrodeposition show an average impedance of 0.56 ± 0.25 megaohm, measured at 1 kilohertz (kHz) (Fig. 3C, blue trace). The PEDOT:PSS-modified microelectrodes demonstrated a statistically significant decrease in impedance values down to 14 ± 7.6 kiloohms, measured at 1 kHz (Fig. 3C, red trace), which is in agreement with previously reported values (*26*). Lower impedance due to PEDOT:PSS coating was consistent before (fig. S3E, pink trace) and after (fig. S3E, green trace) self-rolling of 3D-SR-BAs (no statistically significant difference in impedance, $n = 15$, fig. S3F). These results demonstrate no effect of self-rolling on the performance of sensors. Such low impedance previously resulted in higher signal amplitudes in electrophysiology recordings (*26*).

3D-SR-BAs with active biosensors: GFETs

Graphene, a one-atom-thick 2D honeycomb arrangement of sp^2-hybridized carbon, is a promising building block for bioelectronics due to its exceptional electrical conductivity, superior robustness, mechanical strength and flexibility, high surface area, chemical stability, and ease of tunability (*16*). As a proof of concept of our platform flexibility, GFETs were fabricated on the flexible polymeric surface of the 3D-SR-BAs, as illustrated by the 3D confocal image (fig. S4; see additional information regarding GFET fabrication and characterization in the Supplementary Materials) (*28*–*30*).

Interfaces of 3D-SR-BA with 3D CM spheroids

The 3D-SR-BA is designed to allow recording of electrical activity of tissues in 3D. This type of electrophysiology study assays the electrical activity from all sides of the construct, which allows a more accurate evaluation of electrical signal propagation that cannot be captured with available optical techniques, such as Ca^{2+} imaging. To ensure that the encapsulation of the tissue by 3D-SR-BA does not adversely affect the top layers of cells in the spheroid and the tissue health, the biocompatibility of the platform was evaluated.

Biocompatibility analysis

Biocompatibility of 3D-SR-BAs was tested through cell viability using Live/Dead assay (see Materials and Methods). Five-day-old CM spheroids treated with blebbistatin to decouple excitation and contraction exhibited inhibition of spontaneous cell beating (*31*). The fluorescent staining using the Live/Dead assay and the nuclei stain is illustrated in Fig. 4A, indicating calcein acetoxymethyl (calcein-AM) (green), ethidium homodimer (red), and Hoechst (blue) fluorescent dye staining of the live cells, dead cells, and cell nuclei, respectively. The green fluorescence was used to verify the live cells. Because of the high cell density and cell overlap in a 3D spheroid, we used the blue fluorescently stained nuclei to estimate the total number of live cells (for details, see Materials and Methods). The results indicate that 3D-SR-BA does not negatively affect the encapsulated spheroid. Nonsignificant difference in the % viability between the encapsulated spheroids and the non-encapsulated control spheroids confirms that 3D-SR-BA does not affect cell viability (Fig. 4). Two hours after encapsulation, the % viability shows a statistically significant decline for both the encapsulated spheroids and the non-encapsulated controls compared to viability immediately after encapsulation. This could be attributed to the absence of O_2 and CO_2 gasses in the setup and continuous raster scanning for live-cell imaging. These data lead to the conclusion that the 3D-SR-BAs do not negatively affect the encapsulated spheroids' health.

3D recording from human embryonic stem cell–derived CM spheroids

Embryonic stem cell-derived CM (ES-CM) spheroids compacted in agarose microwells and exhibited spontaneous contraction on day 3 after seeding. Seven-day-old rod-shaped ES-CM spheroids were transferred to a 3D-SR-BA chip with a temperature-controlled Tyrode's solution-filled chamber (see Materials and Methods). Using an *x-y-z* micromanipulator, the arrays were unrolled (movie S2) and each spheroid was successfully encapsulated by a 3D-SR-BA, as illustrated by confocal microscopy image in Fig. 5A. Confocal microscopy imaging indicated that the spheroid was placed in direct contact with the biosensors, which improved the biosensor-cell interface (*16*). Twelve microelectrode biosensors arranged in 3D (Fig. 5B) simultaneously recorded the field potentials (FPs) from the encapsulated CM spheroid (see Materials and Methods). Addition of blebbistatin, a chemomechanical decoupler (*31*), ensured that the motion artifacts, characteristic to CMs, are absent in the FP recording (fig. S5). The low impedance of the microelectrodes led to a signal-to-noise ratio (SNR) as high as ca. 9. The spheroid had a beating rate of ca. 19 beats per minute, which is in good agreement with literature (Fig. 5C) (*32*). Labeling the CMs with a Ca^{2+} indicator, Fluor-4 (Fig. 5A, green fluorescence), allowed simultaneous monitoring of Ca^{2+} transients, as illustrated in Fig. 5A (movie S3). Ca^{2+} transients from the selected marked areas in fig. S6A were analyzed and correspond to the FP recorded from channels 4 and 5 (fig. S6). The Ca^{+2} transient properties, i.e., transient shape and pace, inside and outside of the 3D-SR-BA are similar (fig. S6), thus indicating that the

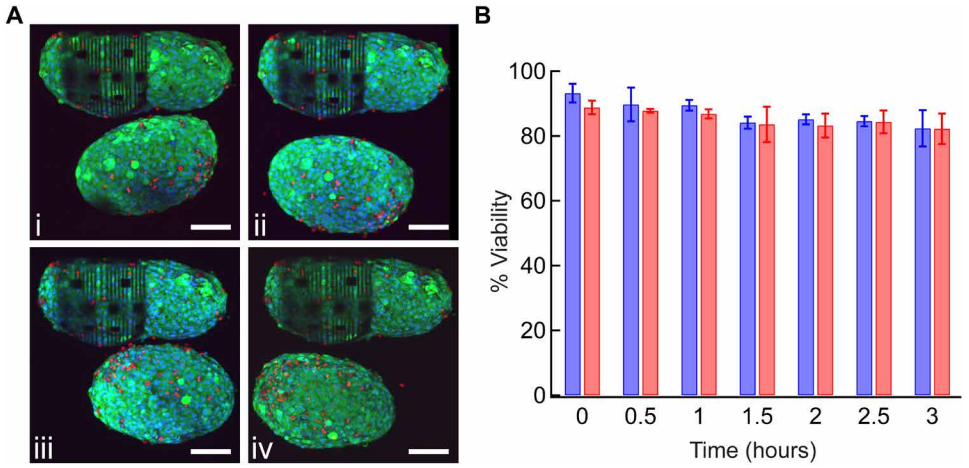

Fig. 4. Effect of 3D-SR-BA on viability of CMs in an encapsulated spheroid. (**A**) Live/Dead assay performed on CM spheroids: a spheroid encapsulated by 3D-SR-BA (top), a spheroid non-encapsulated in 3D-SR-BA (bottom), imaged at (i) 0 hours (immediately after encapsulation), (ii) 1 hour, (iii) 2 hours, and (iv) 3 hours. Green, red, and blue denote live cells, dead cells, and cell nuclei, respectively. Scale bars, 100 μm. (**B**) Viability analysis of spheroids encapsulated by 3D-SR-BA (blue) and not encapsulated spheroid controls (red) that were imaged every 30 min for 3 hours. Results are reported as mean ± SD ($n = 3$). There was no significant difference in the % viability between the encapsulated spheroids and the non-encapsulated control spheroids.

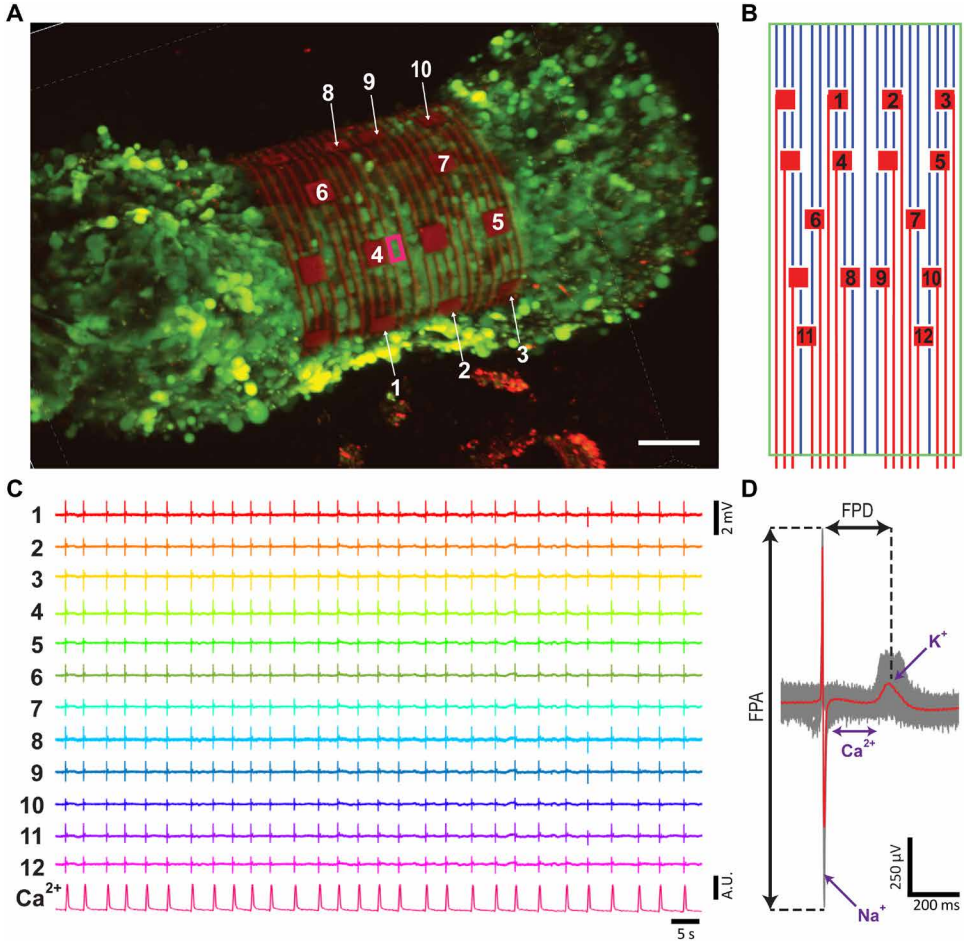

Fig. 5. Electrical recordings in 3D of cardiac spheroids. (**A**) A 3D confocal microscopy image of 3D cardiac spheroid labeled with Ca^{2+} indicator dye (Fluo-4, green fluorescence) encapsulated by the 3D-SR-BA. Scale bar, 50 μm. (**B**) 2D map of the microelectrodes labeled in (A). (**C**) Representative field potential (FP) traces recorded from the channels labeled in (A) and (B). A.U., arbitrary units. Simultaneously recorded Ca^{2+} fluorescence intensity as a function of time of the ROI marked by pink box in (A). (**D**) Averaged FP peak (red trace) and raw data (gray traces, $n = 100$ peaks recorded by channel 4).

sensor arrays do not negatively affect the encapsulated spheroid functionality. The Ca^{2+} transient spike frequency agreed with the FP spike frequency (Fig. 5C and fig. S6B) and is within the range of previously reported values (*15*, *32*). Using electrical biosensors allowed in-depth electrophysiological investigation at a single sensor level (Fig. 5D). The temporal resolution of the electrical recordings using 3D-SR-BA allowed the detection of the individual ionic currents across the cell membrane: Na^+ current (upstroke), K^+ current (repolarization), and Ca^{2+} current (plateau phase), labeled in purple on the recorded traces (Fig. 5D) (*15*). A few details can be gleaned from these data, such as the average recorded FP amplitude (FPA) for representative channel 4 of 1314 ± 25 μV and FP duration (FPD) of 279 ± 29 ms (n = 100 peaks), which agreed with published values (*15*, *32*). Furthermore, the platform was used to obtain stable recordings from the same spheroid for up to 3 hours after spheroid encapsulation (fig. S7).

Although the optical imaging of Ca^{2+} transients was able to provide the beat frequency information, the confocal imaging is limited to an individual x-y plane, not allowing to obtain 3D information with high temporal resolution. 3D-SR-BAs were able to record from CM spheroids with high spatial and temporal resolution in 3D. The time latency between FPs recorded from the spheroid was evident, as illustrated in Fig. 6A. The time latency analysis (see the "Full-field 2D representation of signal delays" section in Materials and Methods) indicates that the FPs recorded by the sixth microelectrode preceded the FPs of the other channels. The time latencies calculated with respect to channel 6 remained consistent throughout the recording (fig. S8A). The fast transient propagation was further examined across all recording channels simultaneously by visualizing relative positive and negative phases of the FP's fast transient, as represented by the 2D map of the sensor with time versus voltage data (Fig. 6B and movie S4). Most evidently, at t = 27.5 ms (Fig. 6B), it is possible to see that while the left-hand side sensors are at their negative phase (blue color), the right-hand side sensors are still at the positive phase (red color). The signal propagation direction in the 3D-rendered representation (Fig. 6C) is indicated by a white arrow. Electrical recordings with 3D-SR-BA exhibit high spatiotemporal resolution, which allows construction of 3D isochronal map of the spheroid's surface (Fig. 6D, a 2D isochronal map representation of the spheroid's 3D surface). Such analysis is impossible using Ca^{2+} transient imaging. The conduction velocity calculated as the gradient from the extrapolated time latency isochronal map (Fig. 6D, white arrow) averaged at 12.45 ± 1.88 cm/s. The conduction velocities of additionally measured spheroids are 6.09 ± 0.65 cm/s (fig. S8D) and 14.55 ± 1.79 cm/s (fig. S8G) for the second and third spheroids, respectively. The signal propagation direction is indicated by the white

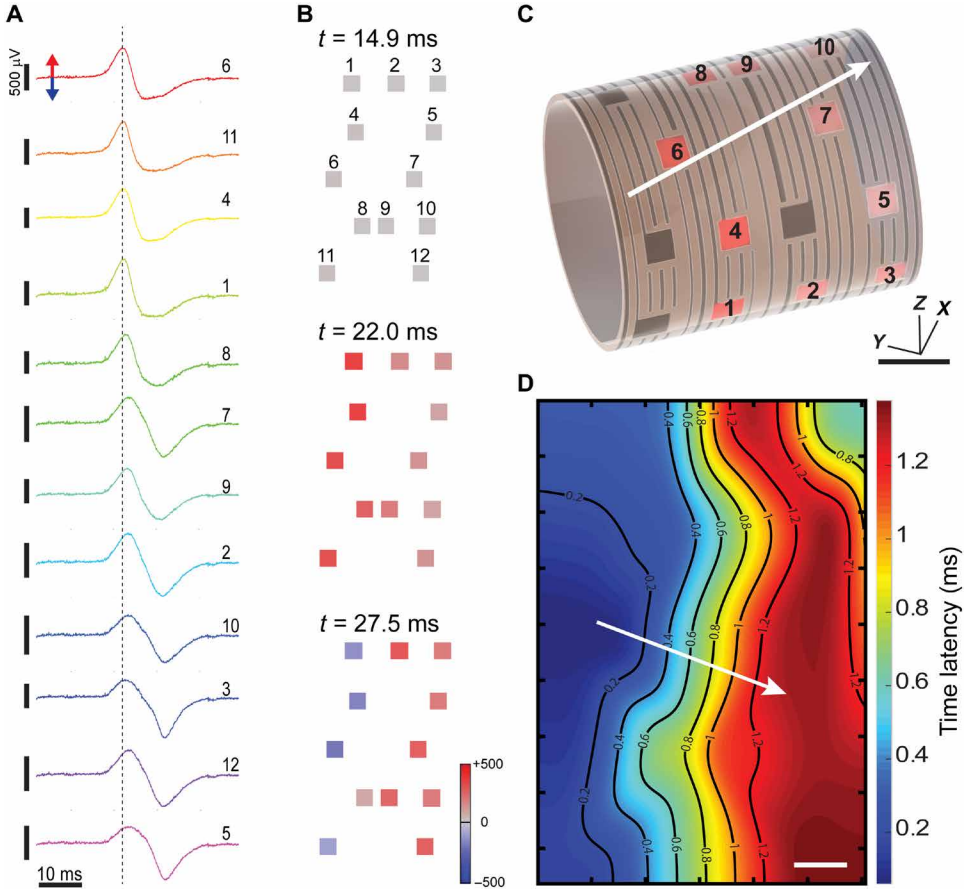

Fig. 6. Mapping electrical signal propagation in 3D using 3D-SR-BA. (**A**) Representative recorded single FP fast transients across 12 channels. Red and blue arrows represent the positive and negative phases of the recorded transients, respectively. (**B**) 2D representation of the fast transient signal phases across all 12 channels. Resting state is presented at t = 14.9 ms, and depolarizing wave propagation is presented at t = 22.0 ms and t = 27.5 ms. (**C**) 3D rendered signal propagation at t = 22.7 ms. Scale bar, 50 μm. (**D**) 2D representation of the isochronal map of time latencies. Scale bar, 35 μm. White arrow in (C) and (D) represents average conduction velocity direction.

arrows in fig. S8. The time latencies remained consistent throughout the independent recording of each spheroid, as illustrated by the calculated SD of the time latencies depicted in fig. S8 (B, E, and H) for spheroids 1, 2, and 3, respectively. Conduction velocity values are in good agreement with the values reported previously (*33*).

Conclusions and future directions

In conclusion, this work demonstrates the first 3D multisite and simultaneous measurements from a 3D multicellular system using 3D-SR-BAs. The highly controlled 3D-SR-BA's geometry allows sensor customization to interface spheroids of varied size. The high spatial resolution of the arrays provided information from individual cells of the spheroid in 3D, while exceptional temporal resolution of the recordings identified ionic currents (Na^+, K^+, Ca^{2+}) in the high SNR FP recordings. Functional assays indicate that the 3D-SR-BAs do not affect the spheroid's functionality. In addition, 3D-SR-BAs show no detectable adverse effect on the viability of the cells. The biocompatibility assay highlights the potential of 3D-SR-BA to be used for stable interfaces with electrogenic spheroids for electrophysiology studies that can last for several hours. High spatiotemporal resolution of the electrical recordings allows following signal propagation in 3D, which is impossible using Ca^{2+} transient imaging.

The proposed 3D-SR-BAs introduce an approach for organ-on-e-chip bioelectronics. A future direction for the 3D-SR-BAs includes incorporation of porosity into the polymeric structures of the platform. This porosity will allow more efficient nutrient diffusion, ensuring long-term viability of spheroids. The 3D-SR-BAs are highly scalable, and the subsequent potential increase in recording density will allow investigation of larger cellular networks. This work shows tailored device diameters to accommodate a range of spheroid sizes that are governed by the limits of diffusion. For larger tissue sizes, a future direction for the 3D-SR-BAs involves scaling up of both the width and the length dimensions, which can be easily attained by addition of force generating metal lines. The use of 3D-SR-BAs for long-term electrophysiological studies of multicellular 3D systems will enable following tissue development and maturation. In addition, it will allow testing of the drug effects on spheroids with diseased and healthy phenotypes. Further capabilities of 3D-SR-BA extend beyond electrophysiology and may combine concurrent electrical measurement and stimulation (enabled by 3D-SR-BAs with passive devices) with biosensing (using highly sensitive active devices, such as GFETs, which will require additional integrated circuit amplification added to the platform) to gain insight into more complex 3D electrogenic tissue constructs.

MATERIALS AND METHODS

3D-SR-BA fabrication

The 3D-SR-BAs were fabricated using well-established microfabrication techniques (*15*). Si substrate with a 600-nm wet thermal oxide (p-type, ≤0.005 ohm·cm, NOVA Electronic Materials Ltd., catalog no. CP02 11208-OX) was cleaned with acetone and isopropyl alcohol (IPA) in an ultrasonic bath for 5 min each, N_2 blow-dried, and treated with O_2 plasma at 100-W power for 1 min (International Plasma Corporation Barrel Asher). The substrate was coated with 300-nm lift-off resist (LOR3A, MicroChem) and 500-nm positive photoresist (Shipley S1805, MicroChem). Outer electrode interconnects were defined by ultraviolet (UV) exposure using a mask aligner (MA6, Karl Suss) followed by development for 1 min in CD26 developer (MicroChem). Cr (10 nm) (99.99%, R.D. Mathis Co.) and Au (75 nm) (99.999%, Praxair) were deposited using a thermal evaporator (Angstrom Engineering Covap II). The LOR3A/Shipley 1805/metal stack was lifted off using Remover PG (MicroChem). The wafer was washed with acetone and IPA, N_2 blow-dried, and treated with O_2 plasma at 50-W power for 1 min. A 200-nm Ge (99.999%, Kurt J. Lesker) sacrificial layer was patterned and deposited similarly. The mechanical support with varied thicknesses (170 to 240 nm) was patterned using negative photoresist (SU-8 2000.5, MicroChem). Using a thinner (SU-8 2000 thinner, MicroChem), the SU-8 was adjusted to 10.7, 9.5, 7.1, and 4.7% solids to achieve a thickness range of 390 to 100 nm. The biosensor array interconnects (sources and drains and microelectrodes for GFETs and MEAs, respectively) were patterned using similar methods as the outer interconnects. Cr (1 nm) (99.998%, Kurt J. Lesker), Pd (50 nm) (99.99%, Kurt J. Lesker), and Cr (25 nm) (99.998%, Kurt J. Lesker) were deposited using an electron beam evaporator (Pro Line PVD Evaporator, Kurt J. Lesker). In the case of MEAs, an additional layer of 10 nm Au (99.999%, Kurt J. Lesker) was deposited. Last, the interconnects and the nonrecording leads of the biosensors were passivated with 100 to 180 nm of diluted SU-8 2000.5. In the case of GFETs, an additional step for graphene transfer and patterning was implemented before the biosensor interconnect patterning and metallization. Low-pressure chemical vapor deposition (LPCVD)–synthesized graphene (see method below) was transferred to device chips and patterned using photolithography and reactive ion etching (RIE), as previously described (*15*). Briefly, LOR3A (300 nm) and Shipley S1805 (500 nm) were coated on substrates with graphene, patterned by UV exposure using a mask aligner, and developed for 1 min in CD26 developer. Excess graphene was etched off by RIE (Plasma-Therm 790) using 14 standard cubic centimeters per minute (sccm) O_2 and 6 sccm Ar at 20-W power and 10-mtorr pressure for 10 s. After etching, the LOR3A/Shipley 1805 stack was stripped off using Remover PG.

Graphene synthesis and transfer

A single layer of graphene was synthesized by a Cu-catalyzed LPCVD process, as previously described (*15*, *34*). Briefly, a 2 cm × 6 cm Cu foil (99.8%, Alfa Aesar, uncoated, catalog no. 46365) was cleaned with acetone and IPA in an ultrasonic bath for 5 min each and then N_2 blow-dried. Before being introduced into a custom-built CVD setup, the foil was treated with a 5.4% (w/w) HNO_3 solution (CMOS grade, J.T. Baker, catalog no. JT9606-3) for 30 s, rinsed three times with deionized (DI) water, and N_2 blow-dried. The synthesis process was carried out at 1050°C and a total pressure of 0.5 torr. The temperature was ramped up to 1050°C in 20 min, followed by stabilization at 1050°C for 5 min under a flow of 100 sccm Ar. The foil was annealed for 60 min under the flow of 100 sccm H_2, followed by a synthesis step of 8 min under the flow of 50 sccm CH_4 (5% in Ar, Airgas) and 100 sccm H_2 (Matheson Gas). The sample was rapidly cooled from growth temperature down to 100°C in 30 min while flowing 100 sccm Ar. The Cu foil with graphene on both sides was cut to the required dimensions. Before Cu etching, one side of the foil was coated with 200 nm of polymethylmethacrylate (PMMA 950 A4, MicroChem) to mechanically support and protect graphene. The graphene on the uncoated side of the foil was etched in a UV-ozone cleaner (PSD Pro Series Digital UV-Ozone, Novascan) for 15 min at 100°C. The Cu foil was wet-etched in a solution containing 25% (w/w) $FeCl_3.6H_2O$ (Sigma-Aldrich, catalog no. 31232), 4%

(w/w) HCl acid (CMOS grade, J.T. Baker, catalog no. BDH3028), and 71% (w/w) DI water. After the Cu etching, the PMMA-supported graphene film was transferred to DI water two times, then to 70% ethanol-water mixture, and finally onto a final substrate (device chip, previously cleaned with acetone, IPA, and N_2 blow-dried). The transferred samples were air-dried overnight. The substrates were then baked at 150°C for 30 min. After the bake, PMMA was dissolved in an acetone bath at 60°C for 30 min. Last, the device chips were rinsed with acetone and IPA and N_2 blow-dried.

Graphene characterization

Raman spectroscopy of graphene was performed with NT-MDT NTEGRA Spectra (100× objective) under 532-nm excitation. For the Raman spectra, a laser power of 2.3 mW was used; the spectra were recorded with an acquisition time of 15 to 30 s. Raman spectra were obtained from within 10 independent GFET channel ribbons as well as directly outside of each ribbon, as illustrated in fig. S4D. Analysis of the acquired spectra was performed using a custom MATLAB (MathWorks Inc.) code to identify characteristics of graphene Raman peaks: Their position, full width at half maximum, and relative peak ratios (table S2).

3D-SR-BA structure release

After fabrication, the 3D-SR-BA chips were cleaned with acetone and IPA and N_2 blow-dried. A rectangular chamber was prepared by using 10:1 base:curing agent polydimethylsiloxane (PDMS) (Sylgard 184 Silicone Elastomer, Dow Corning), cured overnight at 65°C, cut to the needed dimensions, and positioned on a device chip such that the well surrounds the 3D-SR-BA region. A 1% H_2O_2 (Sigma-Aldrich, catalog no. 216763) solution in DI water was added to the well for 1 hour up to overnight to dissolve the Ge sacrificial layer and trigger self-rolling. After 3D-SR-BAs conformed in 3D, the solution in the well was exchanged for DI water.

3D-SR-BA radius of curvature measurements

The radius of curvature was estimated using the 3D reconstruction of confocal images in Nikon NIS Elements software. Briefly, the *y*-*z* plane slices of the *z*-stack were obtained to visualize the circumference of each 3D-SR-BA. The radii were measured by using a three-point circular fit to the 3D-SR-BA circumference slice in NIS Elements software, as illustrated in fig. S2A.

Mechanical simulations

3D FEA with geometric nonlinearities was performed using the commercially available package Abaqus (Dassault Systèmes). The residual stress-induced self-rolling behavior of the 3D-SR-BAs was modeled as a differential thermal expansion–driven shape transformation problem, where hypothetical thermal expansion coefficients were assigned to the constituent layers (*35*). The temperature was gradually raised to such a level that the resultant thermal stresses were equivalent to the residual stresses. A combination of homogeneous (for regions occupied by only SU-8) and composite (for regions patterned with Pd and Cr) shell sections was used in the computations. The thicknesses and material properties of SU-8, Pd, and Cr layers were summarized in table S1. For meshing, the four-node shell element S4R with reduced integration, hourglass control, and finite membrane strains was used. To replicate the experimental design where one end of our 3D-SR-BA was free to roll along the longitudinal axis while the other was physically anchored to the substrate, we applied an unconstrained boundary condition along the edge at one end, and a fully fixed boundary condition was applied at the opposite end.

Electrical characterization of GFETs

GFETs (n = 20) were characterized to ensure ohmic contacts of metal to graphene by recording source-to-drain current (I_{SD}) with varied source-to-drain voltage (V_{SD}) using a source meter unit (2604, Keithley). Three-terminal water-gate measurements were obtained in Tyrode's solution, composed of calcium chloride (0.2 g/liter; anhydrous), magnesium chloride (0.1 g/liter; anhydrous), potassium chloride (0.2 g/liter), sodium chloride (8 g/liter), sodium phosphate monobasic (0.05 g/liter; anhydrous), D-glucose (1 g/liter), and sodium bicarbonate (1 g/liter; Sigma-Aldrich, catalog no. T2145), supplying a linearly increasing gate potential from −0.3 to 0.7 V via Ag/AgCl electrode using a function generator (DG1032, Rigol). The charge neutrality voltage (Dirac point) was determined as the voltage at which the recorded I_{SD} was at minimum. Device sensitivity was determined by taking the first derivative of I_{SD}. The maximum p- and n-type regime sensitivity was determined by the minima and maxima of the sensitivity curve, respectively (fig. S4J).

PEDOT:PSS electrodeposition

Electrodeposition was performed in a three-electrode cell setup using a potentiostat (PalmSens 3, PalmSens). Pt wire, Ag/AgCl electrode, and Au microelectrode were used as counter, reference, and working electrode, respectively. A solution of 0.01 M EDOT (97%, Sigma-Aldrich, catalog no. 483028) (*26*) and 0.02 M PSS (Sigma-Aldrich, catalog no. 243051) was prepared in DI water. Briefly, 53 µl of EDOT was vigorously stirred with 206 mg of PSS in 50 ml of DI water and used as an electrolyte solution. PEDOT:PSS electrodeposition was performed by using a constant current density of 0.5 mA/cm^2 applied for 10 min per electrode.

Electrochemical characterization of microelectrodes

CV experiments were performed in a three-electrode cell setup using a potentiostat, as previously described (*15*). Electrolyte solution of 1 M KCl (≥99%, Sigma-Aldrich, catalog no. P5405) was prepared in DI water. Analyte solution of 5 mM $K_3[Fe(CN)_6]$ (Sigma-Aldrich, catalog no. 244023) was prepared in 1 M KCl solution. Before conducting CV experiments, a PDMS well was sealed to the sample using 10:1 base:curing agent PDMS. Pt and Ag/AgCl electrodes were used for counter and reference electrodes, respectively. To determine the faradaic peaks, we recorded the CV measurements within a potential range from −0.2 to 0.6 V versus Ag/AgCl at 500 mV/s scan rate in the presence of 5 mM $K_3[Fe(CN)_6]$ in 1 M KCl solution. For capacitive currents, CV was conducted with 1 M KCl electrolyte solution within a potential range from −0.2 to 0.3 V versus Ag/AgCl at 600 mV/s scan rate.

EIS was performed in a three-electrode cell setup using a potentiostat (CHI660C, CH Instruments). Phosphate-buffered saline (PBS) (1×) (Thermo Fisher, catalog no. 10010023) was used as an electrolyte solution. Pt wire and Ag/AgCl electrodes were used for counter and reference electrodes, respectively. The frequency was scanned from 0.01 to 100,000 Hz with V_{DC} of 0 V and V_{AC} of 10 mV.

Both CV (n = 10) and EIS experiments (n = 23) were performed before and after PEDOT:PSS electrodeposition. EIS experiments (n = 15) were performed before and after 3D-SR-BA self-rolling on the same electrodes. All measurements were performed in a grounded aluminum box.

Cell culture and CM spheroid formation

Cell culture

Human CMs were differentiated from HUES9 and HES3 human embryonic stem cells (hESCs) using established protocols (*36*). The hESCs were expanded in Essential 8 (E8) medium (Life Technologies, catalog no. A1517001) (*37*) on Geltrex-coated six-well plates (12 μg/cm^2; Life Technologies, catalog no. A1413301) with an initial seeding density of 125,000 cells per well for HUES9 and 100,000 cells per well for HES3 cells. The cells were passaged every 4 days to prevent over-confluence. For CM differentiation, hESCs were seeded at a density of 16,000 cells/cm^2 for HUES9 and 12,000 cells/cm^2 for HES3 cells in E8 medium with 2 μM ROCK inhibitor, thiazovivin (Selleck Chemicals, catalog no. S1459); the medium was changed daily. On the third day after seeding, hESCs were differentiated into CMs. Cells were washed with 1× PBS and incubated with RPMI 1640 medium (Thermo Fisher, catalog no. 21870076) supplemented with B27 minus insulin (Thermo Fisher, catalog no. A1895601) and 1% (v/v) L-glutamine (Thermo Fisher, catalog no. 25030081) plus 6 μM CHIR99021 (LC Laboratories, catalog no. C-6556), a glycogen synthase kinase-3 inhibitor (LC Laboratories, catalog no. S1459), for 2 days. On day 2 of differentiation, cells were washed with 1× PBS and incubated with RPMI/B27 medium and 2 μM Wnt-C59, a Wnt pathway inhibitor (Selleck Chemicals, catalog no. S7037). On days 4 and 6 of differentiation, the medium was changed to RPMI/B27. On days 8 and 10, the medium was changed to CDM3 medium (*37*) consisting of RPMI 1640 medium supplemented with 1% (v/v) L-glutamine, human albumin (500 μg/ml) (Sigma, catalog no. A9731), and L-ascorbic acid 2-phosphate sesquimagnesium salt hydrate >95% (213 μg/ml) (Sigma, catalog no. A8960). On day 12, spontaneously beating cells were passaged for CM purification. CMs were purified using lactate-supplemented medium, which achieves 95 to 98% purification of CMs, as previously demonstrated (*38*). Briefly, beating CMs were washed with 1× PBS and detached from the surface with TrypLE express (Thermo Fisher, catalog no. 12604013) for 15 min at 37°C. Detached cells were pipetted into Dulbecco's modified Eagle's medium (DMEM)/F12 (Thermo Fisher, catalog no. 11320033) and centrifuged at 200*g* for 7 min to pellet the cells. CMs were seeded on Matrigel-coated plates (12 μg/cm^2) (Corning, catalog no. 356231) with RPMI 1640 lacking glucose (Thermo Fisher, catalog no. 11879020) and supplemented with human albumin (500 μg/ml), L-ascorbic acid-2-phosphate (213 μg/ml), and sodium lactate (7.1 mM) (Sigma, catalog no. L4263). CMs were purified for 5 days and then switched back to CDM3 for at least 2 days before passaging.

Spheroid formation

The spheroids were formed following a previously established protocol (*39*). Briefly, sterile solution (10 g/liter) of agarose (Invitrogen, catalog no. 16500) was prepared in 0.9% (w/v) NaCl (Sigma, catalog no. S5886) in DI water. The agarose spherical microwells were obtained by casting the agarose into a mold (3D Petri Dish, Microtissues Inc.). The agarose microwells were equilibrated twice in CDM3 medium for 30 min at 37°C. After purification, adherent CM cultures were lifted with TrypLE for 15 min at 37°C. Cells were pipetted into DMEM/F12 and centrifuged at 200*g* for 7 min. CMs were then seeded at a density of 1.2×10^6 cells/mold for trough-shaped spheroids and 0.65×10^6 cells/mold for round spheroids in 190 μl of CDM3 medium with 2 μM ROCK inhibitor, thiazovivin. The CM spheroids were formed in microwells while incubating at 37°C and 5% CO_2 for 1 day, after which the medium was exchanged to CDM3. The cell medium was changed every other day with a fresh CDM3 medium. After 3 to 5 days, when spheroids compacted and began to spontaneously beat, they were harvested by inverting the micromolds and centrifuging for 5 min at 500 rpm. Spheroids 1 and 2 were formed from HUES9 hESCs, while spheroid 3 and spheroids used for biocompatibility studies were formed from HES3 hESCs.

Encapsulation of spheroids in 3D-SR-BAs

The harvested spheroids were placed in a Tyrode buffer solution–filled recording chamber attached to the 3D-SR-BA chip. Each 3D-SR-BA was unrolled using a micromanipulator (SMX, Sensapex), as illustrated in movie S2, followed by the spheroid encapsulation inside the arrays. After encapsulation, the recording chamber was perfused continuously with fresh Tyrode's solution at 37°C.

Biocompatibility analysis

Cell viability was tested using the Live/Dead Assay Kit (Thermo Fisher, catalog no. L3224) containing calcein-AM and ethidium homodimer dyes for staining live and dead cells, respectively, as previously described (*34*). Spheroids were formed from HES3 CMs and incubated at 37°C and 5% CO_2 for 5 days with CDM3 medium changed every other day. Hoechst 33342 (Thermo Fisher, catalog no. 62249), calcein-AM, and ethidium homodimer dyes were added with a final concentration of 1 μg/ml, 2 μM, and 4 μM, respectively, to each sample and incubated for 30 min at 37°C and 5% CO_2. The spheroids were then treated with 20 μM blebbistatin (Sigma-Aldrich, catalog no. B0560) to decouple excitation and contraction, leading to inhibition of spontaneous cell beating (*31*). The spheroids were washed with Tyrode's solution, and one spheroid was encapsulated by 3D-SR-BA. The live-cell imaging was performed at 37°C using upright confocal microscope (Nikon A1R) under 20×/0.50 numerical aperture (NA) water immersion objective, with perfusion of Tyrode's solution with 4 μM ethidium homodimer dye at 37°C. The spheroid encapsulated by 3D-SR-BA alongside with the non-encapsulated control was imaged immediately after encapsulation and every 30 min after the encapsulation up to 3 hours. The procedure was repeated three times for different sets of spheroids.

% Viability quantification was evaluated as previously described (*34*) using the following formula

$$\%\text{Viability} = \frac{\text{Total cells (blue)} - \text{Dead cells (red)}}{\text{Total cells (blue)}} \times 100$$

where blue refers to the cells stained by Hoechst and red refers to the dead cells stained by ethidium homodimer. Total cell count and dead cell counts were determined by counting the Hoechst- and ethidium homodimer–stained nuclei across the spheroid images for each of the encapsulated spheroid and non-encapsulated control spheroid separately (n = 3 each), using the spot tracking algorithm in Imaris software (Imaris 8.2 Image Visualization and Analysis, Bitplane, Oxford Instruments).

Electrical and optical recordings

Before recording, CM spheroids were stained with the Ca^{2+} indicator Fluo-4 AM. Fluo-4 AM (10 μM) (Thermo Fisher, catalog no. F14217) was prepared in 1× PBS and incubated at 37°C for 30 min. After incubation, the spheroids were washed three times with Tyrode's solution prewarmed at 37°C. Each chip was glued to a printed circuit board (PCB) with soldered 36-pin connector (Omnetics, catalog no. A79024-001). The electrodes on the chip were wire-bonded to

the Cu pads on the PCB using a manual wedge wire bonder (7476D Wire Bonder, West Bond). The chip was loaded onto the microscope stage, and the temperature inside the culture chamber was maintained by constant perfusion of Tyrode's solution maintained at 37°C using an inline heater (ThermoClamp, Automate Scientific). The spheroids were encapsulated by 3D-SR-BAs. After initial set of recordings, the spheroids were treated with 20 μM blebbistatin and additional recording sets were obtained.

For electrical recordings, the Omnetics connector on the PCB was connected to a 32-channel amplifier (Intan Technologies, RHD2132), and the electrical signals were recorded using the Intan acquisition system (Intan Technologies, RHD2000) at an acquisition rate of 20 kHz. The optical recordings were performed using an upright microscope equipped with a resonant confocal scanner (Nikon A1R) under 20×/0.50 NA water immersion objective. All the recordings were performed in a grounded Faraday cage.

Electrical and optical data analysis

The raw data acquired using Intan acquisition software were analyzed using custom-made MATLAB scripts. The beat frequency was calculated using the fast Fourier transform function. The findpeaks function was used to detect the Na^+ peaks, and the FPA was calculated by adding the heights of positive and negative peaks. To measure FPD, we detected Na^+ and K^+ peaks using findpeaks function, and calculated the distance between the peaks. Before using findpeaks function, the voltage versus time curves were smoothened using Savitzky-Golay filtering to avoid interference of the baseline noise while detecting K^+ peaks. To measure the SNR, we divided FPA by the peak-to-peak amplitude of the baseline noise. The peak-to-peak amplitude of the baseline noise was calculated as 6.6 times the SD of the baseline signal acquired for 5 min.

For Ca^{2+} signal analysis, the time-lapse image sequences were imported to a custom MATLAB script. The script provided a maximum intensity projection of the Ca^{2+} image stack, on which the regions of interest (ROIs) were selected. The data from each ROI were averaged for each frame and stored as a time versus intensity series, with time points determined using the frame rate of the image acquisition. The series were then smoothed using a third-order Savitzky-Golay numerical smoothing algorithm with a user-selected window length. The smoothed fluorescence intensity versus time traces were plotted for each ROI.

Wave propagation analysis

2D representation of signal propagation

Using the image measurement tools in ImageJ (National Institutes of Health), the boundaries of each sensor pad were determined using a CAD layout of a 3D-SR-BA (fig. S1B), i.e., *x*, *y* location and the width and height were stored for each pad. A custom MATLAB script used the sensor image as a template for each frame of movie S7. To generate each frame, the voltage data for each recording channel at each time point were placed at all pixel locations identified as being contained by the sensor pad (from ImageJ measurements). The 2D time versus voltage data for each sensor pad were thus expanded into a sequence of *x, y* voltage images constructed through time. The images were generated in the real valued 32-bit .tiff format. The sequence of images was saved individually with a sequential file name. These files were then imported as an image sequence into ImageJ for colorization. The phase lookup table was used to allow for visualization of positive and negative voltages. Time and color-bar overlays were added using ImageJ. The image stack was finally exported as an .avi movie.

3D rendered signal propagation

To generate a 3D representation of the signal propagation at a given time point, we extracted the 2D image of the sensor activity at that time point from the image stack obtained, as described above. The image was then adjusted using Photoshop (Adobe) to remove the background and replace it with transparency and saved as a .png file. The edited image was transferred into Inventor (Autodesk) and applied as a decal wrapped around a cylinder with the dimensions matching a single-turn 3D-SR-BA. A 2D representation of the 3D signal propagation was then exported as a .jpg file.

Full-field 2D representation of signal delays

A custom MATLAB script was used for the following analysis. The recording data for all sensors were split into individual FPs by finding the peak maxima at each FP and extracting a 25-ms window of time before and after each peak. These extracted data segments were used to identify the time delay between each sensor for a given FP. To determine the signal origin and time latencies across the spheroid, the time points of the maxima of FPs for each sensor were compared, and the earliest time point was set as time 0. For each FP, an approximation of the time delays for the entire sensor was constructed by interpolating and extrapolating the time latency using the physical coordinates of the sensor pads and the previously calculated delay values. The approximated surface of time latency calculated for each FP was averaged over all FPs recorded in 1 min of data. A contour map of isochrones was generated using the average time latency surface and the gradient of the delays across the entire measured area. Using this gradient and the average time latency surface, the conduction velocity along the gradient was calculated. Furthermore, the SD of the time latencies at each point within the isochron image was calculated using all FPs recorded in 1 min of data.

Statistical analysis

Data were represented as the mean ± SD. Statistical analysis was performed using Student's *t* test (two-tailed) to determine significant difference between two independent groups with one variable, i.e., impedance before and after PEDOT:PSS deposition, or impedance of the 3D-SR-BAs before and after rolling (fig. S3F). NS denotes no statistically significant difference between two sample populations. A two-way ANOVA followed by Tukey's post hoc test was performed for more than two groups with two independent variables, i.e., encapsulated versus non-encapsulated spheroids, and varied time after encapsulation, i.e., 0.5, 1, 1.5, 2, 2.5, and 3 hours (Fig. 4).

SUPPLEMENTARY MATERIALS

Supplementary material for this article is available at http://advances.sciencemag.org/cgi/content/full/5/8/eaax0729/DC1

Fig. S1. Schematics of the 3D-SR-BA geometry.
Fig. S2. Simulation and experimental results for 3D-SR-BA used to estimate the radius of curvature.
Fig. S3. 3D-SR-BA with microelectrodes: Fabrication and electrochemical characterization.
Fig. S4. 3D-SR-BA with GFETs: Fabrication and electrical characterization.
Fig. S5. Electrical recordings with and without addition of chemomechanical decoupler, blebbistatin.
Fig. S6. Simultaneous Ca^{2+} and electrical recording.
Fig. S7. Several hours (3 hours) 3D recording.
Fig. S8. 3D electrical signal propagation in spheroids.
Table S1. Thickness and mechanical parameters of SU-8, Cr, and Pd used in FEM simulations.
Table S2. Data summary for the Raman analysis of LPCVD synthesized graphene before and after patterning.

Movie S1. Release of the 3D-SR-BA upon sacrificial layer etch.
Movie S2. Unrolling the 3D-SR-BA using a micromanipulator.
Movie S3. Beating CM spheroid stained with Ca^{2+} (Fluo-4) encapsulated in the 3D-SR-BA (associated Ca^{2+} imaging analysis is presented in fig. S6).
Movie S4. Electrical signal propagation in CM spheroid presented in Figs. 4 and 5.

REFERENCES AND NOTES

1. H. R. Irons, D. K. Cullen, N. P. Shapiro, N. A. Lambert, R. H. Lee, M. C. LaPlaca, Three-dimensional neural constructs: A novel platform for neurophysiological investigation. *J. Neural Eng.* **5**, 333–341 (2008).
2. M. C. LaPlaca, V. N. Vernekar, J. T. Shoemaker, D. K. Cullen, Three-dimensional neuronal cultures, in *Methods in Bioengineering: 3D Tissue Engineering*, J. R. Morgan, F. Berthiaume, Eds. (Artech House, 2010), pp. 187–204.
3. M. Hindié, M. Vayssade, M. Dufresne, S. Queant, R. Warocquier-Clérout, G. Legeay, P. Vigneron, V. Olivier, J.-L. Duval, M.-D. Nagel, Interactions of B16F10 melanoma cells aggregated on a cellulose substrate. *J. Cell. Biochem.* **99**, 96–104 (2006).
4. S. A. Maskarinec, C. Franck, D. A. Tirrell, G. Ravichandran, Quantifying cellular traction forces in three dimensions. *Proc. Natl. Acad. Sci. U.S.A.* **106**, 22108–22113 (2009).
5. P. Friedl, K. S. Zänker, E.-B. Bröcker, Cell migration strategies in 3-D extracellular matrix: Differences in morphology, cell matrix interactions, and integrin function. *Microsc. Res. Tech.* **43**, 369–378 (1998).
6. A. Birgersdotter, R. Sandberg, I. Ernberg, in *Seminars in Cancer Biology* (Elsevier, 2005), vol. 15, pp. 405–412.
7. T.-H. Chun, K. B. Hotary, F. Sabeh, A. R. Saltiel, E. D. Allen, S. J. Weiss, A pericellular collagenase directs the 3-dimensional development of white adipose tissue. *Cell* **125**, 577–591 (2006).
8. J. A. Pedersen, M. A. Swartz, Mechanobiology in the third dimension. *Ann. Biomed. Eng.* **33**, 1469–1490 (2005).
9. R. Jain, E. Lammert, Cell–cell interactions in the endocrine pancreas. *Diabetes. Obes. Metab.* **11**, 159–167 (2009).
10. M. A. Lancaster, M. Renner, C.-A. Martin, D. Wenzel, L. S. Bicknell, M. E. Hurles, T. Homfray, J. M. Penninger, A. P. Jackson, J. A. Knoblich, Cerebral organoids model human brain development and microcephaly. *Nature* **501**, 373–379 (2013).
11. B. Sakmann, E. Neher, Patch clamp techniques for studying ionic channels in excitable membranes. *Annu. Rev. Physiol.***46**, 455–472 (1984).
12. M. Scanziani, M. Häusser, Electrophysiology in the age of light. *Nature* **461**, 930–939 (2009).
13. M. Halbach, U. Egert, J. Hescheler, K. Banach, Estimation of action potential changes from field potential recordings in multicellular mouse cardiac myocyte cultures. *Cell. Physiol. Biochem.* **13**, 271–284 (2003).
14. B. Tian, J. Liu, T. Dvir, L. Jin, J. H. Tsui, Q. Qing, Z. Suo, R. Langer, D. S. Kohane, C. M. Lieber, Macroporous nanowire nanoelectronic scaffolds for synthetic tissues. *Nat. Mater.* **11**, 986–994 (2012).
15. S. K. Rastogi, J. Bliley, D. J. Shiwarski, G. Raghavan, A. W. Feinberg, T. Cohen-Karni, Graphene microelectrode arrays for electrical and optical measurements of human stem cell-derived cardiomyocytes. *Cell. Mol. Bioeng.* **11**, 1–12 (2018).
16. S. K. Rastogi, A. Kalmykov, N. Johnson, T. Cohen-Karni, Bioelectronics with nanocarbons. *J. Mater. Chem. B* **6**, 7159–7178 (2018).
17. J. Cools, Q. Jin, E. Yoon, D. Alba Burbano, Z. Luo, D. Cuypers, G. Callewaert, D. Braeken, D. H. Gracias, A micropatterned multielectrode shell for 3D spatiotemporal recording from live cells. *Adv. Sci.* **5**, 1700731 (2018).
18. C. Pitsalidis, M. Ferro, D. Iandolo, L. Tzounis, S. Inal, R. M. Owens, Transistor in a tube: A route to three-dimensional bioelectronics. *Sci. Adv.* **4**, eaat4253 (2018).
19. C. L. Randall, E. Gultepe, D. H. Gracias, Self-folding devices and materials for biomedical applications. *Trends Biotechnol.* **30**, 138–146 (2012).
20. K. Ronaldson-Bouchard, S. P. Ma, K. Yeager, T. Chen, L. Song, D. Sirabella, K. Morikawa, D. Teles, M. Yazawa, G. Vunjak-Novakovic, Advanced maturation of human cardiac tissue grown from pluripotent stem cells. *Nature* **556**, 239–243 (2018).
21. W. Huang, S. Koric, X. Yu, K. J. Hsia, X. Li, Precision structural engineering of self-rolled-up 3D nanomembranes guided by transient quasi-static FEM modeling. *Nano Lett.* **14**, 6293–6297 (2014).
22. I. S. Chun, A. Challa, B. Derickson, K. J. Hsia, X. Li, Geometry effect on the strain-induced self-rolling of semiconductor membranes. *Nano Lett.* **10**, 3927–3932 (2010).
23. N. Bassik, G. M. Stern, M. Jamal, D. H. Gracias, Patterning thin film mechanical properties to drive assembly of complex 3D structures. *Adv. Mater.* **20**, 4760–4764 (2008).
24. G. Guisbiers, O. Van Overschelde, M. Wautelet, Nanoparticulate origin of intrinsic residual stress in thin films. *Acta Mater.* **55**, 3541–3546 (2007).
25. G. Abadias, E. Chason, J. Keckes, M. Sebastiani, G. B. Thompson, E. Barthel, G. L. Doll, C. E. Murray, C. H. Stoessel, L. Martinu, Stress in thin films and coatings: Current status, challenges, and prospects. *J. Vac. Sci. Technol. A* **36**, 020801 (2018).
26. X. Cui, D. C. Martin, Electrochemical deposition and characterization of poly(3,4-ethylenedioxythiophene) on neural microelectrode arrays. *Sens. Actuators B* **89**, 92–102 (2003).
27. A. V. Volkov, K. Wijeratne, E. Mitraka, U. Ail, D. Zhao, K. Tybrandt, J. W. Andreasen, M. Berggren, X. Crispin, I. V. Zozoulenko, Understanding the capacitance of PEDOT: PSS. *Adv. Funct. Mater.* **27**, 1700329 (2017).
28. P. Blake, E. Hill, A. H. Castro Neto, K. S. Novoselov, D. Jiang, R. Yang, T. J. Booth, A. K. Geim, Making graphene visible. *Appl. Phys. Lett.* **91**, 063124 (2007).
29. R. Saito, M. Hofmann, G. Dresselhaus, A. Jorio, M. S. Dresselhaus, Raman spectroscopy of graphene and carbon nanotubes. *Adv. Phys.* **60**, 413–550 (2011).
30. D. Kireev, M. Brambach, S. Seyock, V. Maybeck, W. Fu, B. Wolfrum, A. Offenhäusser, Graphene transistors for interfacing with cells: Towards a deeper understanding of liquid gating and sensitivity. *Sci. Rep.* **7**, 6658 (2017).
31. M. Kovács, J. Tóth, C. Hetényi, A. Málnási-Csizmadia, J. R. Sellers, Mechanism of blebbistatin inhibition of myosin II. *J. Biol. Chem.* **279**, 35557–35563 (2004).
32. C. Robertson, D. D. Tran, S. C. George, Concise review: Maturation phases of human pluripotent stem cell-derived cardiomyocytes. *Stem Cells* **31**, 829–837 (2013).
33. S. A. Thompson, P. W. Burridge, E. A. Lipke, M. Shamblott, E. T. Zambidis, L. Tung, Engraftment of human embryonic stem cell derived cardiomyocytes improves conduction in an arrhythmogenic in vitro model. *J. Mol. Cell. Cardiol.* **53**, 15–23 (2012).
34. S. K. Rastogi, G. Raghavan, G. Yang, T. Cohen-Karni, Effect of graphene on nonneuronal and neuronal cell viability and stress. *Nano Lett.* **17**, 3297–3301 (2017).
35. H. Hu, C. Huang, X. H. Liu, K. J. Hsia, Thin film wrinkling by strain mismatch on 3D surfaces. *Ext. Mech. Lett.* **8**, 107–113 (2016).
36. X. Lian, J. Zhang, S. M. Azarin, K. Zhu, L. B. Hazeltine, X. Bao, C. Hsiao, T. J. Kamp, S. P. Palecek, Directed cardiomyocyte differentiation from human pluripotent stem cells by modulating Wnt/β-catenin signaling under fully defined conditions. *Nat. Protoc.* **8**, 162–175 (2013).
37. G. Chen, D. R. Gulbranson, Z. Hou, J. M. Bolin, V. Ruotti, M. D. Probasco, K. Smuga-Otto, S. E. Howden, N. R. Diol, N. E. Propson, R. Wagner, G. O. Lee, J. Antosiewicz-Bourget, J. M. C. Teng, J. A. Thomson, Chemically defined conditions for human iPSC derivation and culture. *Nat. Methods* **8**, 424–429 (2011).
38. S. Tohyama, F. Hattori, M. Sano, T. Hishiki, Y. Nagahata, T. Matsuura, H. Hashimoto, T. Suzuki, H. Yamashita, Y. Satoh, T. Egashira, T. Seki, N. Muraoka, H. Yamakawa, Y. Ohgino, T. Tanaka, M. Yoichi, S. Yuasa, M. Murata, M. Suematsu, K. Fukuda, Distinct metabolic flow enables large-scale purification of mouse and human pluripotent stem cell-derived cardiomyocytes. *Cell Stem Cell* **12**, 127–137 (2013).
39. A. P. Napolitano, D. M. Dean, A. J. Man, J. Youssef, D. N. Ho, A. P. Rago, M. P. Lech, J. R. Morgan, Scaffold-free three-dimensional cell culture utilizing micromolded nonadhesive hydrogels. *Biotechniques* **43**, 494–500 (2007).

Acknowledgments: We would like to thank Jonathan Rivnay for helpful discussions regarding this work. We would like to thank Carnegie Mellon University Nanofabrication Facility and the Department of Materials Science and Engineering Materials Characterization Facility (MCF 677785). **Funding:** T.C.-K. would like to thank the National Science Foundation (CBET1552833) and the Office of Naval Research (N000141712368). C.H. would like to acknowledge financial support from Nanyang Technological University (start-up grant M4082352.050). C.H. and K.J.H. acknowledge partial support by the NIH Eunice Kennedy Shriver National Institute of Child Health and Human Development (grant R01HD086325).
Author contributions: T.C.-K., E.M., S.K.R., and A.K. designed the experiments. E.M., S.K.R., and A.K. performed the experiments. T.C.-K. and A.K. analyzed the data. C.H., A.A., and K.J.H. performed mechanical simulation. S.K.R. assisted with GFET and MEA fabrication and characterization, and electrophysiological recordings. A.W.F. provided the needed hESC-CM expertise for this study. J.B. cultured the hESC-CM. J.T. and D.S. assisted in signal propagation analysis. S.S. assisted in 3D-SR-BA design and fabrication. T.C.-K., A.K., C.H., K.J.H., J.B., D.S., J.T., S.K.R., and A.W.F. wrote the manuscript. All authors read the manuscript and approved it.
Competing interests: The authors declare that they have no competing interests. **Data and materials availability:** All data needed to evaluate the conclusions in the paper are present in the paper and/or the Supplementary Materials. Additional data related to this paper may be requested from the authors.

Submitted 22 February 2019
Accepted 12 July 2019
Published 23 August 2019
10.1126/sciadv.aax0729

Citation: A. Kalmykov, C. Huang, J. Bliley, D. Shiwarski, J. Tashman, A. Abdullah, S. K. Rastogi, S. Shukla, E. Mataev, A. W. Feinberg, K. J. Hsia, T. Cohen-Karni, Organ-on-e-chip: Three-dimensional self-rolled biosensor array for electrical interrogations of human electrogenic spheroids. *Sci. Adv.* **5**, eaax0729 (2019).

Science Advances

Organ-on-e-chip: Three-dimensional self-rolled biosensor array for electrical interrogations of human electrogenic spheroids

Anna Kalmykov, Changjin Huang, Jacqueline Bliley, Daniel Shiwarski, Joshua Tashman, Arif Abdullah, Sahil K. Rastogi, Shivani Shukla, Elnatan Mataev, Adam W. Feinberg, K. Jimmy Hsia and Tzahi Cohen-Karni

Sci Adv **5** (8), eaax0729.
DOI: 10.1126/sciadv.aax0729